

A multiphase tracking method for modelling the interfacial flow of two immiscible liquids in mixing process

H. Tang ^{*}, J.Y. Tu ^{*}, L.C. Wrobel [†],

27 September 2004

Abstract

This paper presents an interface tracking method for modelling the flow of immiscible metallic liquids in mixing processes. The methodology can provide an insight into mixing processes for studying the fundamental morphology development mechanisms for immiscible interfaces. The VOF method employed here utilises the piecewise linear for interface construction scheme as well as the continuum surface force algorithm for surface force modelling. A model coupling numerical and experimental data is established. The main flow features in the mixing process are investigated. It is observed that the mixing of immiscible metallic liquids is strongly influenced by the viscosity of the system, shear forces and turbulence. The numerical results show good qualitative agreement with experimental results, and are useful for optimising the design of mixing casting processes.

1 Introduction

Casting immiscible engineering alloys is a challenging problem due to metallic and hydrodynamic phenomena which take place during the process; various research efforts are still in progress to develop a process methodology for obtaining a fine and uniformly dispersed microstructure. Evidence shows that the liquid-liquid decomposition and spatial behaviour in the molten state dominate the solidified microstructure of immiscible alloys. However, the hydrodynamic behaviour in the molten state is not well

^{*}School of Aerospace, Mechanical and Manufacturing Engineering, RMIT University, Victoria, 3083, Australia

[†]School of Engineering and Design, Brunel University, Uxbridge, Middlesex, UB8 3PH, UK

understood. Experiments encounter some difficulties to provide a complete insight into the process. Therefore, a computational method has been developed to investigate the hydrodynamic behaviour of immiscible metallic alloys in a novel casting process called rheomixing, based on the use of a twin-screw extruder (TSE).

2 Process of microstructure evolution

A rheomixing process was developed based on previous experience in the processing of semisolid metal (SSM) slurry by a TSE [1]. TSE is commonly used in polymer processing [2, 3], and provides sufficient shear flow in the rheomixing process to create a fine and homogeneous droplet dispersion, and enough viscous force in the semisolid state to counterbalance the Stokes and Marangoni motions. However, there are still some limitations for the experiments to provide an insight into the flow during the process.

Applications of TSE in immiscible engineering alloy processing generate different flow mechanisms, which result in the desired solidified microstructure of the immiscible engineering alloy. The study of immiscible Zn-Pb binary alloys in shear-induced turbulent flows is important to provide more detailed information into the rheomixing process, to increase our control of the rheology of an emulsion and its solidified microstructure. An understanding of the fluid dynamics inside and around a suspended drop is necessary for delineating the mechanisms of microscopic transport and microstructure of immiscible alloys.

3 Modelling approaches

The solidified microstructure of immiscible alloys strongly depends on processing conditions, especially the liquid-liquid decomposition and spatial separation behaviour within the molten state. There have been several attempts to model at least parts of the microstructure evolution in the liquid state or even the whole process from nucleation until the formation of layers. Two approaches were described in a review paper on immiscible liquid alloys [4]. However, there are more numerical approaches for multiphase flows available to simulate possible phase segregation, coagulation, collision, immiscible interface, sedimentation, etc. These include the dissipative particle dynamics (DPD) approach for the phase segregation of binary systems at the mesoscale, the Euler-Euler approach for macrostructural modelling, various immiscible interface tracking approaches for both microstructural and macrostructural modelling, molecular dynamics (MD) approaches for the simulation in the atomistic scale, as well as combined approaches. Here, the volume-of-fluid (VOF) method is adopted in the present study.

3.1 VOF interface tracking method

The VOF model is a surface-tracking technique applied to a fixed Eulerian mesh. It is designed for two or more immiscible fluids where the position of the interface between the fluids is of interest. In the VOF model, a single set of momentum equations is shared by the fluids, and the volume fraction of each of the fluids in each computational cell is tracked throughout the domain.

As the VOF method provides the possibility of tracking immiscible interfaces that are of interest to the present study, it is employed here for the numerical investigation of the hydrodynamic behaviour of immiscible metallic alloys in the rheomixing process..

The numerical methods adopted in the present simulations are based on Hirt and Nichols' VOF method [5] coupled with Youngs' piecewise linear interface construction (PLIC) scheme [6], Brackbills' continuum surface force (CSF) model [7], and solved by an algebraic multigrid (AMG) solver [8], as well as the k - ϵ turbulence model [9] and the pressure-implicit with splitting of operators (PISO) scheme for pressure-velocity coupling [10].

3.2 The volume evolution equations

In the VOF method, the motion of the interface between immiscible liquids of different density and viscosity is defined by a phase indicator – the volume fraction function C , and the interface is tracked by the following three conditions:

$$C_k(x, y, z, t) = \begin{cases} 0 & \text{(outside } k^{\text{th}} \text{ fluid)} \\ 1 & \text{(inside } k^{\text{th}} \text{ fluid)} \\ >0, <1 & \text{(at the } k^{\text{th}} \text{ fluid interface)} \end{cases}$$

According to the local value of C_k , appropriate properties and variables are assigned to each control volume within the domain.

The volume fraction function C_k is governed by the volume fraction equation:

$$\frac{\partial C_k}{\partial t} + \mathbf{u} \cdot \nabla C_k = 0 \quad (1)$$

where \mathbf{u} is the flow velocity.

The two-phase fluid flows are modelled with the Navier-Stokes equation

$$\rho \left(\frac{\partial \mathbf{u}}{\partial t} + \mathbf{u} \cdot \nabla \mathbf{u} \right) = -\nabla p + \mu \nabla^2 \mathbf{u} + \rho \mathbf{g} + F \quad (2)$$

where F stands for body forces, \mathbf{g} for gravity acceleration, and p for pressure. The velocity field is subject to the incompressibility constraint, $\nabla \cdot \mathbf{u} = 0$.

In a two-phase system, the properties appearing in the momentum equation are determined by the presence of the component phase in each control volume. The average values of density and viscosity are interpolated by the following formulas

$$\rho_{i,j} = \rho_1 + C_2(\rho_2 - \rho_1) \quad (3)$$

$$\mu_{i,j} = \mu_1 + C_2(\mu_2 - \mu_1) \quad (4)$$

In multi-phase systems, the “onion skin” technique is used [11].

3.3 The interface reconstruction algorithm

In the PLIC method, the interface is approximated by a straight line of appropriate inclination in each cell. A typical reconstruction of the interface with a straight line in cell (i, j) , which yields an unambiguous solution, is perpendicular to an interface normal vector $\mathbf{n}_{i,j}$ and delimits a fluid volume matching the given $C_{i,j}$ for the cell. A unit vector \mathbf{n} is determined from the immediate neighbouring cells based on a stencil $C_{i,j}$ of nine cells in 2D. The normal vector $\mathbf{n}_{i,j}$ is thus a function of $C_{i,j}$, $\mathbf{n}_{i,j} = \nabla C_{i,j}$. Initially, a cell-corner value of the normal vector $\mathbf{n}_{i,j}$ is computed. An example at $i+1/2, j+1/2$ in 2D is as follows:

$$\mathbf{n}_{x, i+1/2, j+1/2} = \frac{1}{2h} (C_{i+1,j} - C_{i,j} + C_{i+1,j+1} - C_{i,j+1}) \quad (5)$$

$$n_{y, i+1/2, j+1/2} = \frac{1}{2h} (C_{i,j+1} - C_{i,j} + C_{i+1,j+1} - C_{i+1,j}) \quad (6)$$

The required cell-centred values are given by averaging:

$$n_{i,j} = \frac{1}{4} (n_{i+1/2, j-1/2} + n_{i-1/2, j-1/2} + n_{i+1/2, j+1/2} + n_{i-1/2, j+1/2}) \quad (7)$$

The most general equation for a straight line on a Cartesian mesh with normal $\mathbf{n}_{i,j}$ is

$$n_x x + n_y y = \alpha \quad (8)$$

The normal vector $\mathbf{n}_{i,j}$ is defined by the vector gradient of $C_{i,j}$, which can be derived from different finite-difference approximations which directly influence the accuracy of algorithms. These include Green-Gauss, volume-average, least-squares, minimization principle, Youngs' gradients, as discussed in [12]. It is noted that a wide, symmetric stencil for $\mathbf{n}_{i,j}$ is necessary for a reasonable estimation of the interface orientation.

3.4 The fluid advection algorithm

During an advection step, the volume fraction $C_{i,j}$ is truncated by the formula:

$$C_{i,j} = \min[1, \max(C_{i,j}^f, 0)] \quad (9)$$

at the (n+1) time step. Once the interface is reconstructed, the velocity at the interface is interpolated linearly and the new position of the interface is calculated by the following formula:

$$\mathbf{x}^{n+1} = \mathbf{x}^n + \mathbf{u}(\Delta t) \quad (10)$$

The new $C_{i,j}$ field is obtained according to the local velocity field, and fluxes ΔC at each cell are determined by algebraic or geometric approaches. Here, the simplest operator split advection (geometric) algorithm is used as proposed by [6]:

$$\hat{C}_{i,j} = C_{i,j}^n + \frac{\Delta t}{\Delta x} [F_{i-1/2,j} - F_{i+1/2,j}] \quad (11)$$

$$C_{i,j}^{n+1} = \hat{C}_{i,j} + \frac{\Delta t}{\Delta y} [\hat{G}_{i,j-1/2} - \hat{G}_{i,j+1/2}] \quad (12)$$

where $F_{i-1/2,j} = (Cu)_{i-1/2,j}$ denotes the horizontal flux of the (i,j) cell and $G_{i-1/2,j} = (Cv)_{i,j-1/2}$ denotes the vertical flux of the (i,j) cell. That is, volume fractions are updated at time level n from $C_{i,j}^n$ to $\hat{C}_{i,j}$ with an x sweep, then updated from $\hat{C}_{i,j}$ to $C_{i,j}^{n+1}$ with a y sweep.

3.5 Surface force model

Surface tension along an interface arises as the result of attractive forces between molecules in a fluid. In a droplet surface, the net force is radially inward, and the combined effect of the radial components of forces across the entire spherical surface is to make the surface contract, thereby increasing the pressure on the concave side of the surface. At equilibrium in this situation, the opposing pressure gradient and cohesive forces balance to form spherical drops. Surface tension acts to balance the radially inward inter-molecular attractive force with the radially outward pressure gradient across the surface.

Here, surface tension is applied using the CSF scheme [7]. The addition of surface tension to the VOF method is modelled by a source term in the momentum equation. The pressure drop across the surface depends upon the surface tension coefficient σ ,

$$\Delta p = \sigma \left(\frac{1}{R_1} + \frac{1}{R_2} \right) \quad (12)$$

where R_1, R_2 are the two radii, in orthogonal directions, to measure the surface curvature. In the CSF formulation, the surface curvature is computed from local gradients in the surface normal at the interface. The surface normal \mathbf{n} is defined by

$$\mathbf{n}_{i,j} = \nabla C_{i,j} \quad (13)$$

where $C_{i,j}$ is the secondary phase volume fraction.

The curvature $\kappa_{i,j}$ is defined in terms of the divergence of the unit normal $\hat{\mathbf{n}}$:

$$\kappa = \nabla \cdot \hat{\mathbf{n}} = \frac{1}{|\mathbf{n}|} \left[\left(\frac{\mathbf{n}}{|\mathbf{n}|} \cdot \nabla \right) |\mathbf{n}| - (\nabla \cdot \mathbf{n}) \right] \quad (14)$$

where

$$\hat{\mathbf{n}} = \frac{\mathbf{n}}{|\mathbf{n}|} \quad (15)$$

The surface tension can be written in terms of the pressure jump across the interface, which is expressed as a volume force F added to the momentum equation

$$F_{i,j} = \sigma_{1,2} \kappa_{i,j} \frac{\rho_{i,j} \nabla C}{1/2 (\rho_1 + \rho_2)} \quad (16)$$

where the volume-averaged density $\rho_{i,j}$ is given by Equation (3).

4 Application of PLIC-VOF for immiscible alloy flows

Numerical simulation seems to have some advantages to investigate immiscible flows at the microscopic level. Therefore, a computer modelling technique based on computational fluid dynamics (CFD) coupled with a PLIC-VOF module is applied to solve the problems of decomposition, spatial phase separation and microstructural evolution during the cooling of an alloy through the liquid miscibility gap.

The thermophysical properties of immiscible metallic Pb-Zn binary alloys are taken from [13], while phase equilibrium data are taken from [14]. Shear rate is estimated by the equation $\dot{\gamma} = 2n \pi (r_s / \delta - 1)$, where r_s is the screw radius, n is the screw rotation speed and δ is the gap between barrel and screw surface [15]. Simulations are conducted on simplified flow fields under shear-induced force, which was implemented as moving boundaries in the computational domain coupled with imposed initial flow field condition. The breakup scale factors (BSF) $K_n^t \sim f(L_d, L_p, t)$ (L_d, L_p - characteristic length scales of daughter droplet and parent drop, respectively) are proposed here to measure the size of the daughter drop with $t = \xi$, $t = \psi$, $t = \zeta$ the time for first daughter drop formation, full breakup up of parent drop, and good distribution of daughter droplets, respectively.

4.1 Tracking droplet formation

The results of numerical simulations for one-sided shear-induced flow are shown in Figure 1. The first droplets were formed around 3.6 ms, and the size of the smallest droplet is quite small. The droplet formation occurred in the sheared layer, the wave of the Pb phase appeared first at the time 2.0 ms, followed by a protruding finger at the time 3.2 ms. The protruding finger then broke up, and droplets formed at the time 3.6 ms

The simulations ended after the formation of the first few droplets, due to the limitations of computational facilities. For further simulations, a single drop in shear-

induced flow is considered in order to examine the microstructural mechanism of drop break-up, which will be discussed in the next section.

4.2 Tracking a drop breakup into droplets

The breakup scale factor (BSF) K_r^ξ is defined as the ratio of the capillary number of daughter drop to parent drop, $K_r^\xi = Ca_d / Ca_p = (\dot{\gamma} r_{dd} \mu_m / \sigma) / (\dot{\gamma} r_d \mu_m / \sigma)$, in which r_{dd} denotes the daughter drop radius.

The breakup scale factor (BSF) K_L^ξ is defined as the ratio of the elongative length of the parent drop to the original parent drop diameter, $K_L^\xi = L_D / D_d$, at the time the first daughter drop is formed.

For one-sided shear-induced flows, case 1, $K_r^\xi = 0.083$, while the ratio of the elongative length to the parent drop radius is $K_L^\xi = 2.167$. For two-sided shear-induced flows, results of the simulations are similar to case 1.

Daughter drops were born on both sides as shown in Figure 2, case 2 and case 3. The ratio of the first daughter radius to the parent drop radius K_r^ξ is equal to 0.0125, while the ratio of the elongative length to the parent drop diameter K_L^ξ is equal to 3.417 for case 2. For case 3, the ratio of the first daughter radius to the parent drop radius K_r^ξ is 0.333, the ratio of the elongative length to the parent drop diameter K_L^ξ is 5.542. Case 1 and case 3 need longer for breakup than case 2

The effect of viscosity is illustrated in Fig. 3 through case 4 and case 5. The initial breakup factor $K_r^\xi = 0.167$, $K_L^\xi = 3.833$ for case 4, and $K_r^\xi = 0.125$, $K_L^\xi = 2.667$ for case 5. Case 4 reaches the full breakup much faster than case 5, and the shape of daughter drops in case 5 is longer than in case 4. It appears that the breakup is easier in thin viscous fluids than in thick viscous fluids. This means that the breakup should be completed in the fluid state with low viscosity of the matrix phase in order to obtain fine droplets and short processing time.

4.3 Tracking droplets mixing flow

The breakup scale factor (BSF) K_{\max}^t is defined as the ratio of the largest size of daughter drop to parent drop diameter at each time interval, $K_{\max}^t = r_{dd\max} |_{t=i} / D_d$, $r_{dd\max}$ denotes the largest daughter drop size, D_d denotes the diameter of the parent drop. K_{\min}^t is similar. The interaction behaviour of daughter droplets involves coalescence and refinement as shown in Figure 4 for case 1 and Figure 5 for case 2. It is noted that the range is narrower in one-sided shearing flow (case 1), which is the main flow characteristic of the TSE process.

5 Conclusions

Numerical simulations have been conducted as simplified problems through the VOF method with the PLIC scheme, AMG approach and $k-\varepsilon$ turbulence model. The metallic drop deformation and rupturing, the essential microscopic mechanisms of the rheomixing process, were investigated to increase our understanding of the basic

behaviour of immiscible metallic drops in a prototypical rheomixing process. The results show that numerical methods are capable of simulating the rheological behaviour of an immiscible Zn-Pb binary alloy in shear-induced mixing processes, which reflect the fundamental flow features of twin-screw rheomixing process.

Acknowledgements: We are grateful to researchers in the CFD group in SAMME, RMIT University and SED, Brunel University for helpful discussions on numerical approaches and the TSE rheomixing casting process.

References

- [1] S. Ji, Z. Fan, M.J. Bevis, 2001 Semi-solid processing of engineering alloys by a twin-screw rheomoulding process, *Mat. Sci. Eng. A* **299** (2001) 210-217.
- [2] N.P. Cheremisinoff, *Polymer Mixing and Extrusion Technology*, Marcel Dekker, New York, 1987.
- [3] C. Rauwendaal, *Mixing in Polymer Processing*, Marcel Dekker, New York, 1991.
- [4] L. Ratke, S. Diefenbach, Liquid immiscible alloys, *Mat. Sci. Eng.* **RI5** (1995) 263-347
- [5] C.W. Hirt, B.D. Nichols, Volume of fluid VOF for the dynamics of free boundaries, *J. Comput. Phys.* **39** (1981) 201.
- [6] D.L. Youngs, Time-dependent multi-material flow with large fluid distortion, in: *Numerical Methods for Fluid Dynamics*, K.W. Morton and M.J. Baines (eds.), New York Academic Press, p273–285,1982.
- [7] J.U. Brackbill, D.B. Kothe, C. Zemach, A continuum method for modeling surface tension, *J. Comput. Phys.* **100** (1992)335-354.
- [8] K. Stüben, A review of algebraic multigrid, *J. Comput. Appl. Math.* **128** (2001) 281-309.
- [9] B.E. Launder, D.B. Spalding, The numerical computation of turbulent flows, *Comput. Meth. App. Mech. Engng.* **3** (1974)267-289.
- [10] R.I. Issa, A.D. Gosman, A.P. Watkins, The computation of compressible and incompressible recirculating flows by a non-iterative implicit scheme, *J. Comput. Phys.* **93** (1991) 388-410.
- [11] D.L. Youngs, Time-dependent multi-material flow with large fluid distortion, in: *Numerical Methods for Fluid Dynamics*, K.W. Morton and M.J. Baines (eds.), New York Academic Press, p273–285,1982.
- [12] D.B. Kothe, W.J. Rider, S.J. Mosso, J.S. Brock, Volume tracking of interface having surface tension in two and three dimensions, in: *34th Aerospace Science Meeting and Exhibition*, AIAA96-0859,1996.

- [13] T. Iida, R.I.L. Guthrie, The Physical Properties of Liquid Metals, Oxford University Press, New York, 1988.
- [14] R. Hultgren, R.L. Orr, P.D. Anderson, K.K. Kelley, Selected Values of the Thermodynamic Properties of Binary Alloys, Metals Park, ASM, 1973.
- [15] C. Rauwendaal, Polymer Extrusion, 3rd rev. ed, Hanser, New York, p181,1994.

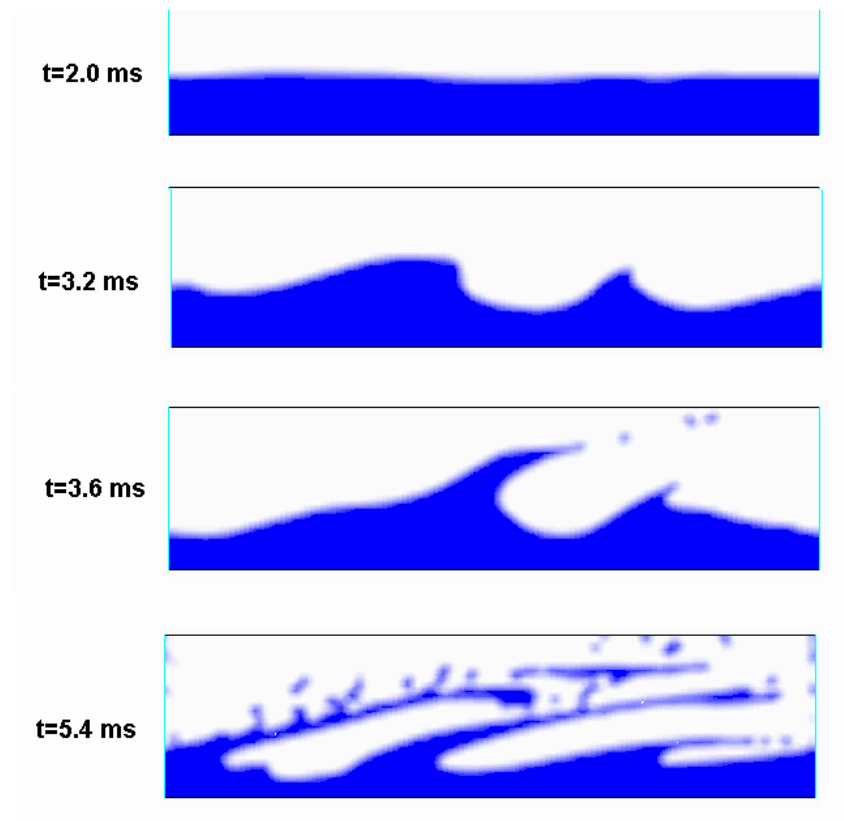


Figure 1: Numerical evaluation of droplet formation in a 2D one-sided shear-induced flow.

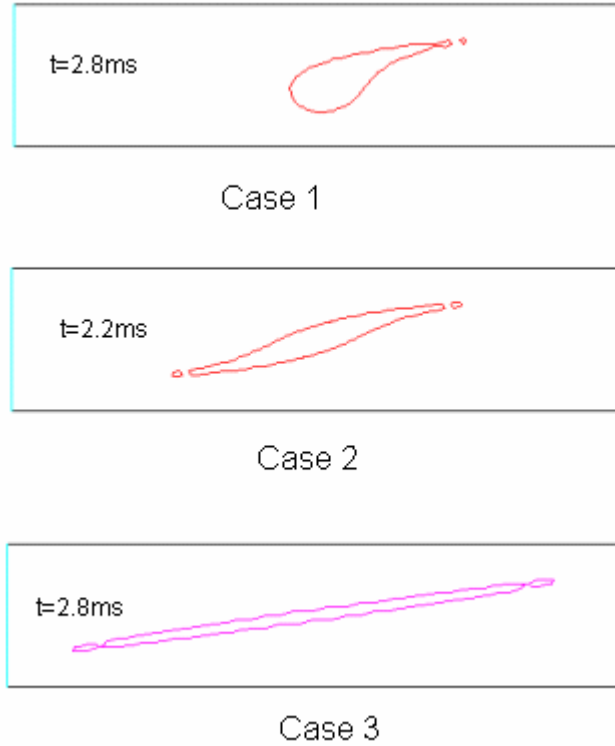


Figure 2 Tracking a drop breakup, grid 128×32 , domain 16×4 , case 1 and case 2 are for $\lambda=1$, $Ca=3.2$ for one side shear-induced flow and double side shear-induced flow respectively and with enhanced initial shear rate near wall. Case 3 is for $Ca=1.17$, $Re=0.0$ initial flow field.

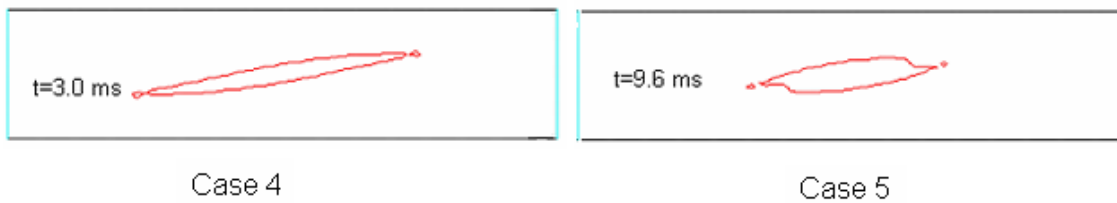


Fig. 3: Tracking a drop breakup, grid 128×32 , domain 16×4 , $Ca=2.5$. Case 4 is for $\lambda=1$, case 5 is for $\lambda=0.5$

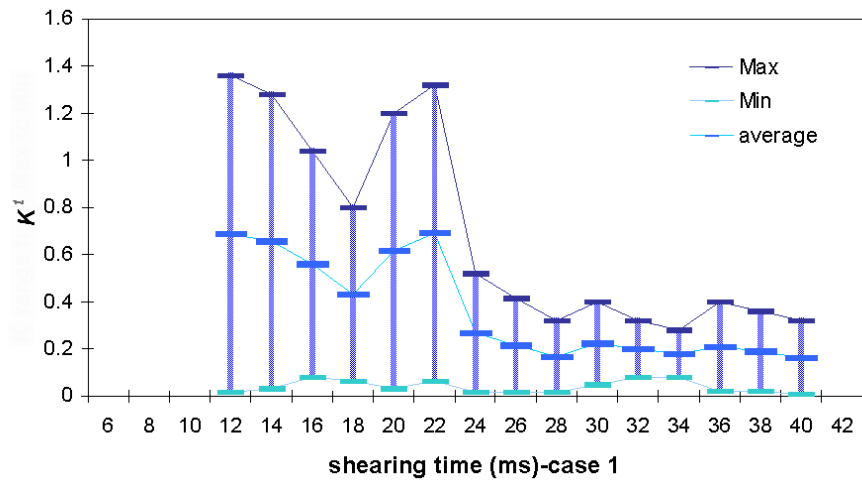


Figure 4: Schematic illustration of K^t range for case 1

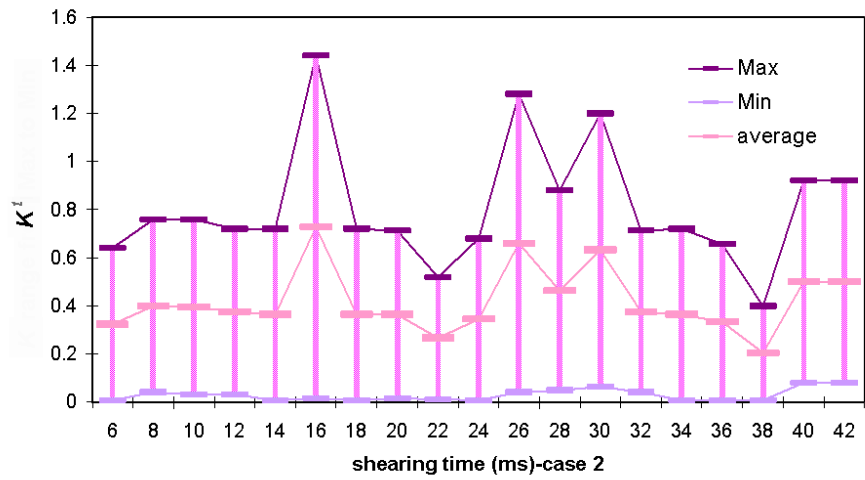


Fig. 5: Schematic illustration of K^t range for case 2